Supplementary Information for

Unraveling the Critical Impact of Anisotropic La Motion on Methane Dissociation over the La_2O_3 (001) Surface

Feiyang Ren,[1,2] *and Qiang Fu* [1,2,3,*]

[1] Hefei National Research Center for Physical Sciences at the Microscale, University of Science and Technology of China, Hefei 230026, China

[2] Hefei National Laboratory, University of Science and Technology of China, Hefei 230088, China

[3] School of Future Technology, University of Science and Technology of China, Hefei 230026, China

*Corresponding author: qfu3@ustc.edu.cn

Energy transfer analysis

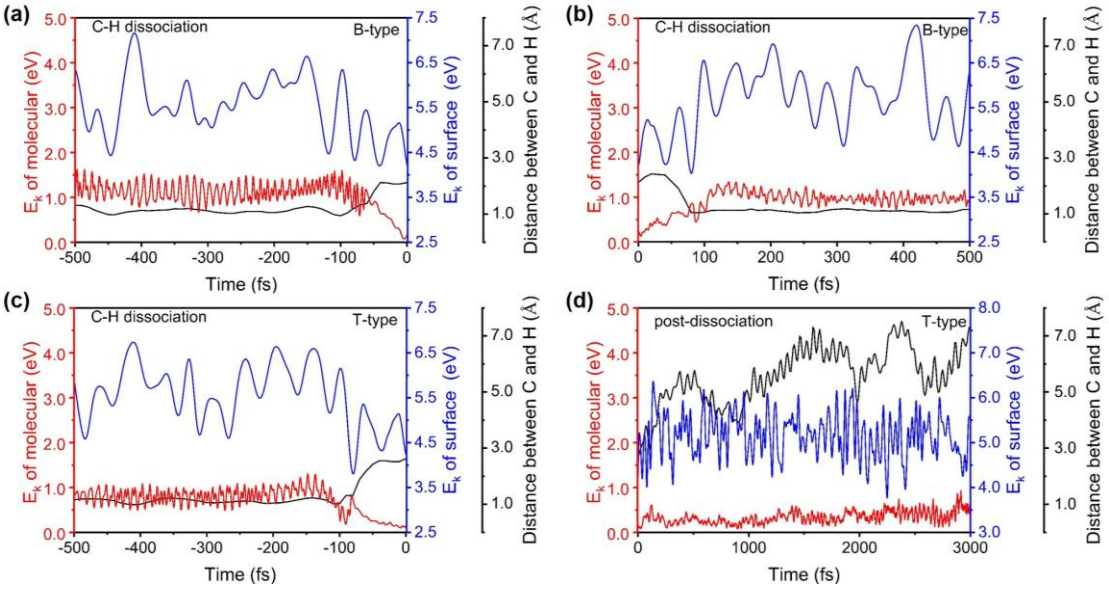

Figure S1: Time evolution of the kinetic energy of the $CH_3\cdots H$ species (red lines), kinetic energy of La_2O_3 surface atoms (blue lines), and distance between the C and H atoms (corresponding to the dissociating C−H bond, gray lines) for the pre-transition-state (a, c) and post-transition-state (b, d) dissociation processes, respectively. Results for the B-type and T-type pathways are shown in (a, b) and (c, d), respectively.

We have investigated the energy transfer between the CH_4 reactant and the $La_2O_3(001)$ surface in the entire dissociation process. AIMD simulations are carried out in the micro canonical (NVE) ensemble, and the transition state structures of CH_4 dissociation (along both the B-type and T-type pathways) are used as the initial configurations (see Supporting Information for more details). We investigate the time evolution of three key quantities: the kinetic energy of the $CH_3\cdots H$ species, the kinetic energy of La_2O_3 surface atoms, and the distance between the C and H atoms (corresponding to the dissociating C−H bond) during CH_4 dissociation. The results are shown in Figure S1. In Figures S1a and S1c, we present CH_4 dissociation processes toward the transition states for the B-type and T-type pathways, respectively, obtained by time-reversing the backward trajectories (toward the reactant CH_4). It can be seen that both pathways exhibit remarkably similar behavior. As the C−H bond elongates (gray lines), the kinetic energy of the $CH_3\cdots H$ species (red lines) decreases, consistent

with the endothermic nature of this process. More importantly, the kinetic energy of the $La_2O_3(001)$ surface atoms (blue lines) decrease simultaneously, demonstrating that energy transfer occurs from the catalyst surface to the reactant species. However, in the post-transition-state dissociation processes, the B-type and T-type pathways exhibit significant differences, as shown in the comparison between Figures S1b and S1d. For the B-type case, the dissociated CH_3^- and H^+ rapidly recombine (manifested by the decreasing C−H distance), and the kinetic energies of both the $CH_3\cdots H$ species and La_2O_3 surface atoms increase simultaneously, demonstrating energy transfer from the recombining CH_4 species to the La_2O_3 surface. For the T-type case, the dissociated CH_3^- continues diffusing on the sur face, resulting in the effective separation between CH_3^- and H^+. The overall increasing trend in the kinetic energy of the CH_3^- species during the sustained diffusion (Figure S2), particularly after 2 ps, indicates further energy transfer from the La_2O_3 surface to CH_3^-, likely for supplying energy to maintain its diffusion. Since it has been found that the branching ratio between the B-type and T-type pathways can be modulated by the upward displacement of the surface La cations, the catalyst-reactant energy transfer dynamics can also be adjusted accordingly.

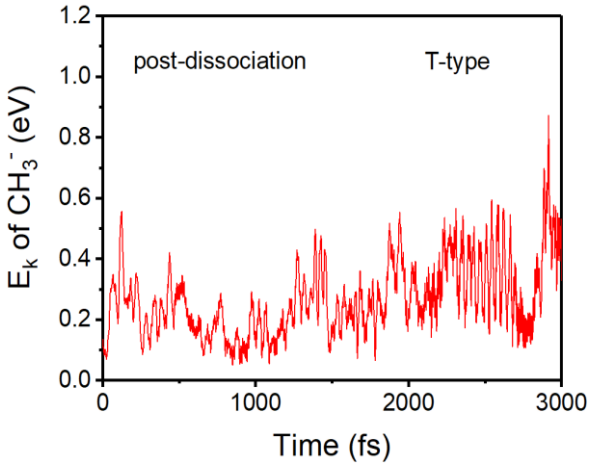

Figure S2. Time evolution of the kinetic energy of the CH_3^- species along the T-type pathway after the transition state has been overcome.

Anisotropic La^{3+} motion on La_2O_3(011) surface

We have also examined the La_2O_3 (011) surface and found that the upward displacement of La^{3+} persists on this facet as well. Our AIMD simulations at 873 K reveal a maximum upward displacement of 0.96 Å, which is notably larger than the movements observed in the downward (0.40 Å), x- (0.58 Å), and y-directions (0.60 Å). The results confirm that the anisotropic upward motion of surface La^{3+} is not limited to the (001) surface.

Other calculation results

Table S1. Optimized atomic layer spacing of La_2O_3 (001) surface using VASP and CP2K, respectively.

Atomic layer	CP2K	VASP
1 and 2	0.63	0.63
2 and 3	1.55	1.55
3 and 4	1.52	1.51
4 and 5	0.67	0.64
5 and 6	1.80	1.79

Table S2. Calculated energy cost and the force on the La^{3+} using VASP and CP2K, respectively, when the La^{3+} is lifted by 0.6 Å (since the forces on the lifted La^{3+} in the x and y directions are close to zero, only the forces in the z-direction are compared).

	VASP	CP2K
Force (eV/Å)	-1.93	-1.98
ΔE (eV)	0.71	0.73

Table S3. Calculated maxima (MAX) of the amplitudes of La^{3+} displacements along different directions on the $La_2O_3(001)$ surface at 873 K using the (3×3) supercell and the (6×6) supercell, respectively.

supercell	MAX (Å)			
	z-up	z-down	x	y
3×3	0.98	0.43	0.57	0.56
6×6	1.01	0.47	0.60	0.58

Table S4. Calculated maxima (MAX) of the amplitudes of the La^{3+} displacements along different directions on the $La_2O_3(001)$ surface at 500 K and 1400 K.

T (K)	MAX (Å)			
	z-up	z-down	x	y
500	0.59	0.25	0.31	0.27
1400	1.12	0.54	0.71	0.69

Table S5. Calculated maxima (MAX) of the amplitudes of the La^{3+} and O^{2-} displacements along different directions on the $La_2O_3(001)$ surface at 873 K.

ion	MAX (Å)			
	z-up	z-down	x	y
La^{3+}	0.98	0.43	0.57	0.56
O^{2-}	0.99	1.02	0.78	0.76

Table S6. Changes in the calculated Bader charge of La^{3+} and O^{2-} when the surface La^{3+} cation is upward displaced by 0.4 Å.

	La^{3+}	O^{2-}
ΔCharge (|e|)	0.010	0.004

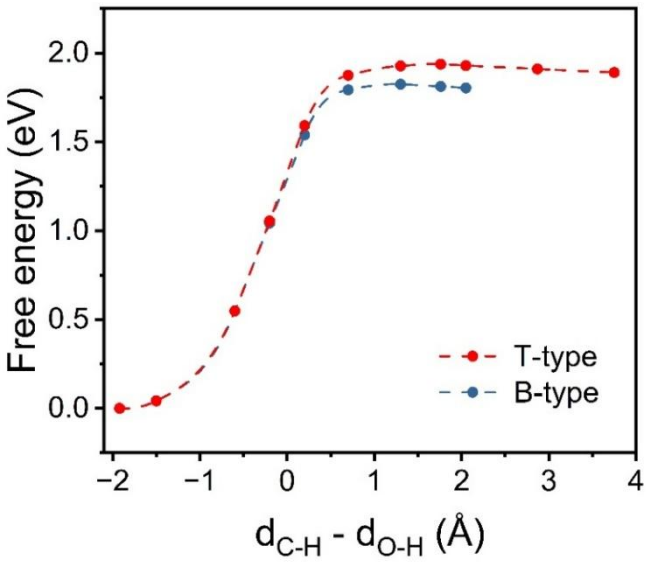

Figure S3. Calculated free energy profiles obtained from c-AIMD simulations for the dissociation of CH_4 at 873 K along the T- type (red line) and B-type (blue line) pathways.

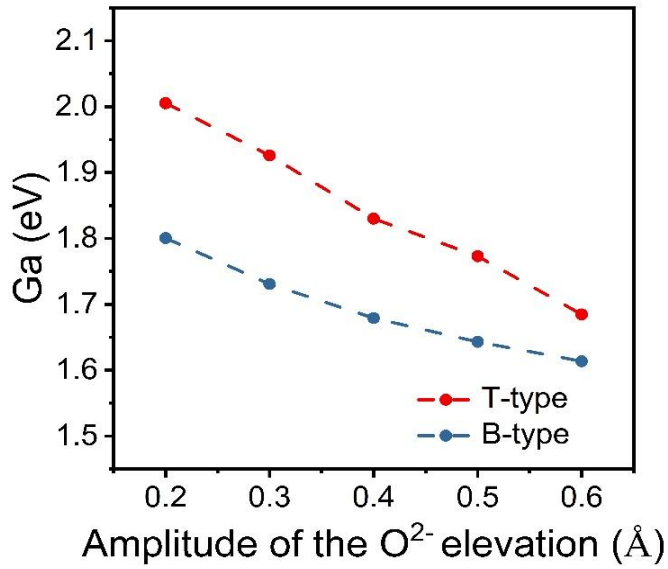

Figure S4. Calculated free energy barriers for the C−H bond cleavage of methane along the T-type (red line) and B-type (blue line) pathways at 873 K, respectively, when a surface O^{2-} anion is vertically lifted by different amplitudes. The free energy barriers are calculated using CI-NEB combined with *ab initio* thermodynamics analysis.

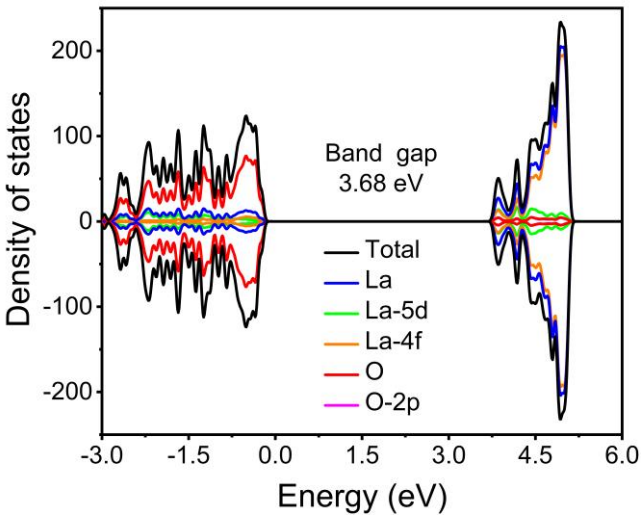

Figure S5. Calculated density of states of the La_2O_3 (001) surface.

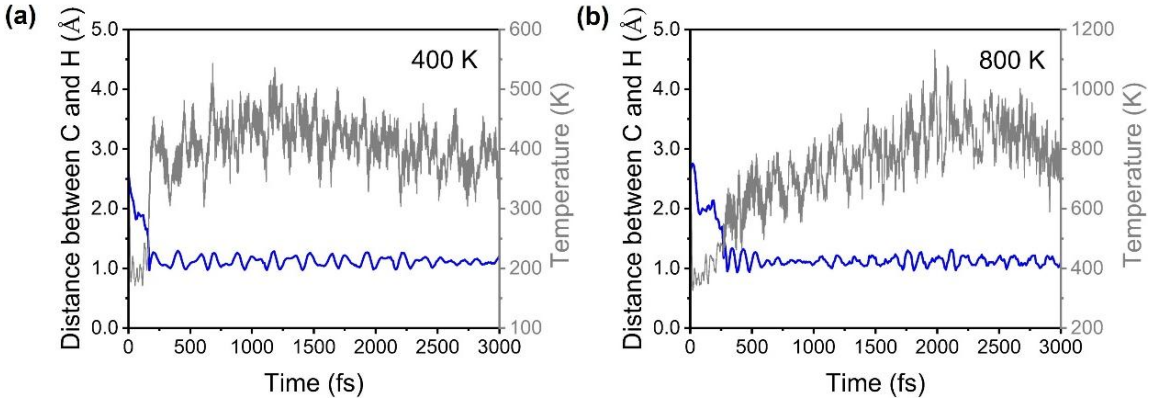

Figure S6. Changes in the distance (blue lines) between the C and H atoms of a dissociated C-H bond for the dissociation product of the B-type pathway from the AIMD trajectories obtained at 400 K (a) and 800 K (b). The changes in the temperature are shown by gray lines.

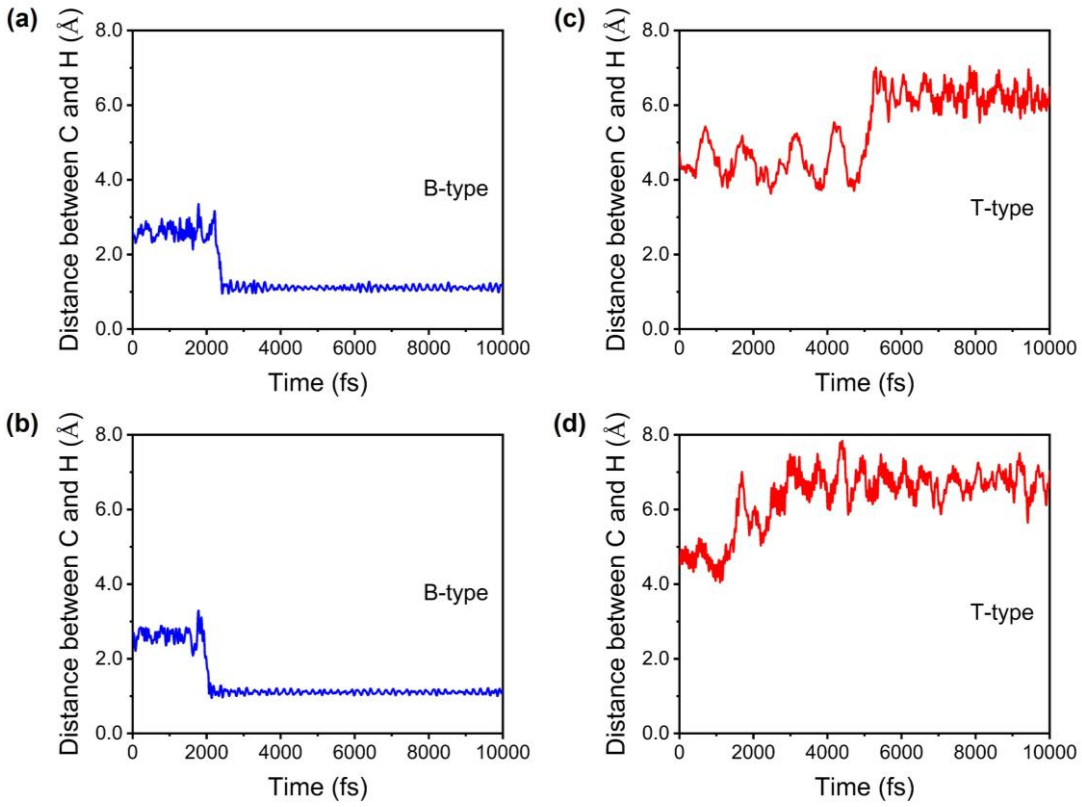

Figure S7. Changes in the distance between the C and H atoms of a dissociated C-H bond for the dissociation products of the B-type (a, b) and T-type (c, d) pathways from two AIMD simulations using different initial velocities. The temperature of the AIMD simulations is set to 250 K.

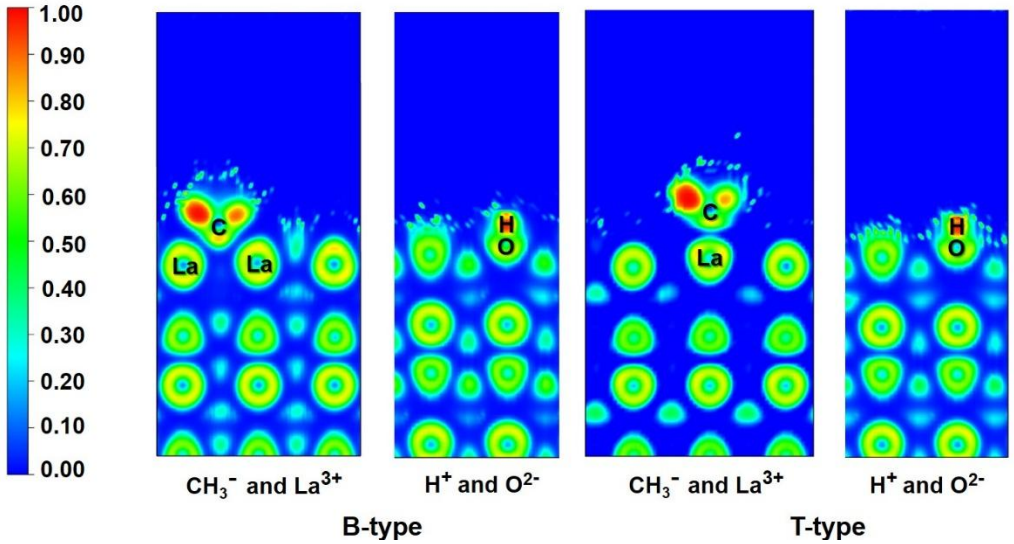

Figure S8. Calculated electron localization function (ELF) of the adsorption configurations of CH_3^- and H^+ adsorbed on La^{3+} and O^{2-}, respectively, formed by CH_4 dissociation via the B-type and T-type pathways.

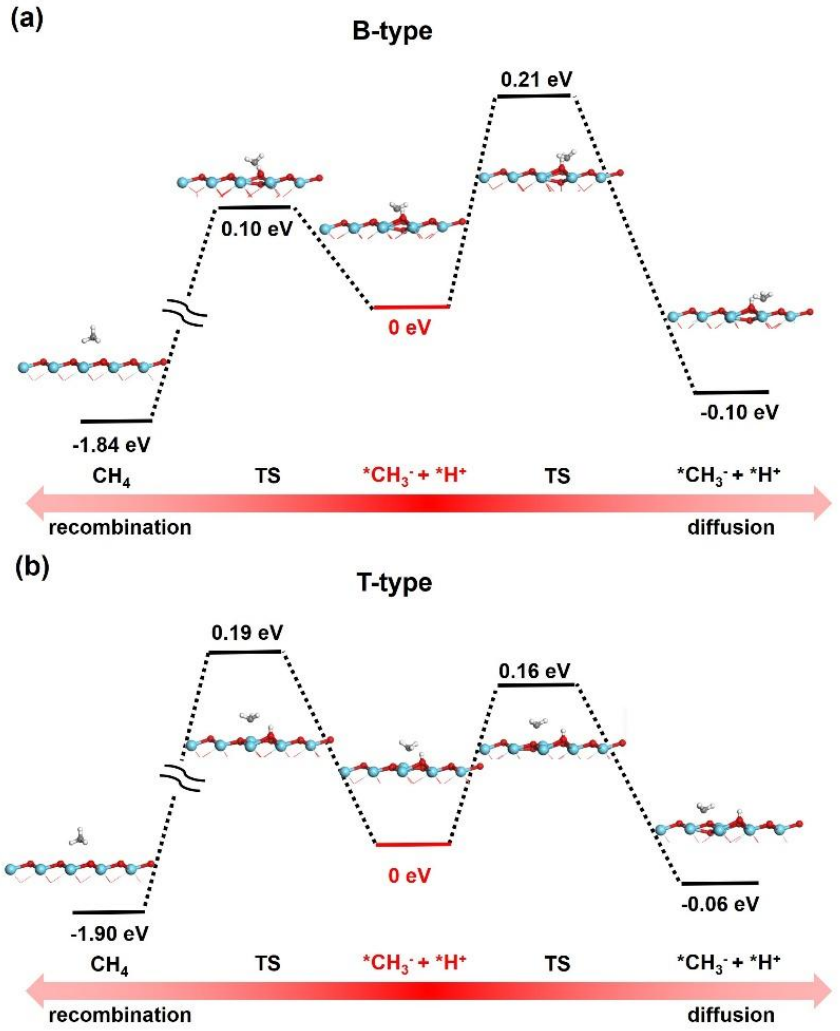

Figure S9. Calculated free energy profiles of both the recombination of CH_3^- and H^+ and the diffusion of CH_3^- for the dissociated products via the B-type (a) and T-type (b) pathways on the $La_2O_3(001)$ surface at 873 K. The side views of all configurations are shown here.